*Submitted to*

*Sensors and Actuators A: Physical*

# *Machine Learning Microfluidic based platform: Integration of Lab-on-Chip devices and data analysis algorithms for Red Blood Cell plasticity evaluation in Pyruvate Kinase Disease monitoring*

*A. Mencattini [1,2], V. Rizzuto [3,4], G. Antonelli [1,2], D. Di Giuseppe [1,2], M. D'Orazio [1,2], J. Filippi [1,2], M.C. Comes [1,2], P. Casti [1,2], J.L. Vives Corrons [3], M. Garcia-Bravo [5,6], J.C. Segovia [5,6], Maria del Mar Mañú-Pereira [7], M.J. Lopez-Martinez [3,8,9], J. Samitier [3,8,9], and E. Martinelli [1,2]**

1. Department of Electronic Engineering, University of Rome Tor Vergata, Via del Politecnico 1, 00133 Rome, Italy
2. Interdisciplinary Center for Advanced Studies on Lab-on-Chip and Organ-on-Chip Applications (ICLOC), Via del Politecnico 1, 00133 Rome, Italy
3. Institute for Bioengineering of Catalonia (IBEC) Barcelona Institute of Science and Technology BIST, Barcelona, 08028, Spain.
4. Josep Carreras Leukaemia Research Institute (IJC), Badalona, 08916, Spain and with University of Barcelona, Department of Medicine, Barcelona, 08036, Spain
5. Biomedical Innovation Unit, Centro de Investigaciones Energéticas, Medioambientales y Tecnológicas (CIEMAT) and Centro de Investigación Biomédica en Red de Enfermedades Raras (CIBERER), Madrid, Spain,
6. Unidad Mixta de Terapias Avanzadas. Instituto de Investigación Sanitaria Fundación Jiménez. (IIS-FJD, UAM). Madrid, Spain.
7. Vall d'Hebron Research Institute, Erithropatology Unit, Translational Research in Child and Adolescent Cancer – Rare anemia disorders research laboratory, Vall d'Hebron Research Institute, ERN-EuroBloodNet member, Barcelona, 08035, Spain
8. Centro de Investigacion Biomedica en Red en Bioingeniería, Biomateriales y Nanomedicina (CIBER-BBN), Madrid, 28029, Spain, University of Barcelona, Department of Electronic and Biomedical Engineering, Barcelona, 08028, Spain.
9. University of Barcelona, Department of Electronic and Biomedical Engineering, Barcelona, 08028, Spain

---

*Correspondence to:*

*Prof. Eugenio Martinelli*

*Department of Electronic Engineering*

*University of Rome Tor Vergata*

*Via del Politecnico 1, 00133 Roma, Italy*

*Email: martinelli@ing.uniroma2.it*

*Tel: +39 06 72597259*

*Fax: +39 06 2020 519*

***Abstract***

Microfluidics represents a very promising technological solution for conducting massive biological experiments. However, the difficulty of managing the amount of information available often precludes the wide potential offered. Using machine learning, we aim to accelerate microfluidics uptake and lead to quantitative and reliable findings. In this work, we propose complementing microfluidics with machine learning (MLM) approaches to enhance the diagnostic capability of lab-on-chip devices. The introduction of data analysis methodologies within the deep learning framework corroborates the possibility of encoding cell morphology beyond the standard cell appearance. The proposed MLM platform is used in a diagnostic test for blood diseases in murine RBC samples in a dedicated microfluidics device in flow. The lack of plasticity of RBCs in Pyruvate Kinase Disease (PKD) is measured massively by recognizing the shape deformation in RBCs walking in a forest of pillars within the chip. Very high accuracy results, far over 85%, in recognizing PKD from control RBCs either in simulated and in real experiments demonstrate the effectiveness of the platform.

***Keywords:*** *machine learning microfluidics, deep transfer learning, video analysis, blood disease*

## *1. Introduction*

Today, one of the most challenging frontiers in system engineering is the possibility of recapitulating limited parts and activities of the human body in ex-vivo environments [1]. This is made possible by microfluidic devices. Microfluidic and Lab-on-a-chip (LOC) technologies [2-4] have attracted increasing interest in recent years. They deal with the fabrication of silicon/plastic microdevices with channels and chambers, and with control of the flow behavior of small volumes of fluids in microchannels and micro-chambers, with dimensions from tens to hundreds of micrometers. Microfluidic devices allow for the mimicking of some crucial biological events such as drug-related cell death (apoptotic events) [5], cell-cell interaction (cancer-immune crosstalk) [6], cell migration patterns [7] and lack of plasticity of the cell [8-10]. LOC systems naturally bring synergy with machine learning approaches, leading to a novel multidisciplinary discipline called machine learning microfluidics (MLM). The MLM branch comprises several aspects, including cell culture, LoC design, time-lapse microscopy, image analysis, and patient stratification [11-17].

MLM platform relies on the possibility of using the same platform for very diverse experimental scenarios [18-22], leading to the extraction of a multitude of quantitative information related to the morpho-kinematics of the moving objects (cell, bacteria, inert compounds, etc.) [23]. On the other hand, MLM systems allow parallelization of experiments in multiple wells implemented on the same chip [24], opening the way to massive high-throughput analysis [25].

To validate the MLM approach, a challenging scenario as the identification of blood diseases in murine red blood cells (RBCs) samples in a dedicated microfluidics device in-flow, has been considered. Actually, the biophysical properties of RBC provide potential biomarkers for the quality of donors or for patient health control as demonstrated in [26,35]. To increase the potential of investigating RBC deformability, sophisticated microfluidic platforms and optical components have been used [27, 36-40]. Some works [41, 42] deal with RBCs in adhesion and propose to analyze static morphological aspects by shape feature and DL.

Bulk flow methods measure the deformability of thousands of cells in a bulk RBC sample, but cannot detect changes in deformability in a small fraction of abnormal cells in a sample containing primarily normal RBCs. Traditional single-cell technologies (e.g., micropipette aspiration, optical tweezers, atomic force microscopy, etc..), have similar sensitivities to the

bulk flow techniques but suffer from greatly reduced throughputs, requiring specialized personnel. Microfluidic techniques combine the benefits of traditional bulk and single-cell techniques – providing higher throughput with equal or greater sensitivity, as well as single-cell measurements. Microfluidics outcomes may be performed through blending with imaging and machine learning (ML) techniques [28].

The potential of using ML in combination with microfluidics is the possibility of enriching the robustness of the analysis and its repeatability. ML allows not only processing massive numbers of cells and, therefore, providing more statistically reliable results, but also, through dedicated preprocessing, to increase the robustness of the analysis to unpredictable variations and inter-experiment heterogeneity due to set-up changes. Furthermore, ML allows to combine the results acquired at single-cell level in a cooperative logic, mimicking the ability of a panel of human experts to take decisions.

More specifically, the main scope of our work is to design a general-purpose MLM system capable of dealing with the non-stationarity of the video sequences acquired and maintaining high diagnostic performance in biological case studies. In particular, with respect to the results shown in [9], here we introduced several modifications to the analysis to address the problems and limitations that occurred in previous work. Techniques such as background subtraction and image sequence equalization were implemented to increase the recognition performance, in addition to inpainting image analysis algorithm required to digitally remove structural parts of the chip, such as pillars, that may confound the cell localization. Furthermore, we proposed a novel learning paradigm based on a two-threshold strategy, to combine the classification label assigned to each single cell in a whole label for each single experiment. Finally, to demonstrate the capability of the MLM platform to distinguish RBCs with lack of plasticity from healthy ones, we first ran artificial experiments with generated frames of moving RBCs applying rotation and deformation models from the literature and estimated the classification accuracies for the different levels of plasticity simulated.

The proposed approach has been validated in an automatic diagnostic test for Pyruvate Kinase Disease (PKD), a hereditary metabolic disorder caused by the lack of pyruvate kinase activity specifically in RBCs [29-32]. PKD constitutes a disease model in which microfluidics could constitute a valid tool to better understand the variability among

patients as well as their response to splenectomy by helping on finding new mechanical biomarkers of the disease [33]. In this work, PKD RBCs have been analyzed versus Wild Type (WT) RBCs from murine samples [34].

## 2. *Methods*

The proposed MLM platform of analysis consists of several steps (see Fig. 1), from sample preparation to the final classification result for a given experiment. First, cells are cultured, and then they are injected into the LOC and put inflow. After cells are forced to deform to pass the slit barriers (dimensions in order of capillaries), they cross the forest of pillars that serve as soft obstacles for RBCs, introducing a less stressed source of deformation. We believe that such a minor source may preserve the plasticity study from bias due to the suck effect and related slipstream that appears when the barrier is completely plugged by a multitude of passing RBCs. The forest of pillars, designed to avoid microchannels collapsing when PDMS is bonded to glass, also mimics the reticular mesh of the spleen that anticipates the area of splits (the fence-like barrier).

Through time-lapse microscopy, a video sequence of the moving cells through the compartment containing the pillars is then acquired and stored in a PC for offline analysis. The data processing step (right section of Fig. 1), based on image processing and machine learning algorithms, aims to provide a diagnostic result for RBCs from comparative biological conditions, healthy vs. unhealthy. Peripheral blood was collected from the tail vein of AcB55 recombinant (PKD) or C57BL/6 (Wild Type, WT) adult mice, and RBCs were obtained after centrifugation to separate them from plasma. Further details can be found in the Supplementary Material. The microfluidic device was fabricated using photo- and soft-lithography. The master mold was obtained from a silicon wafer by patterning polymeric structures using photolithographic techniques. The LoC consisted of eight parallel microchannels containing each a row of funnel-shaped micro-constriction to mimic the filtering function of the red pulp's spleen and a matrix of pillars all along to mimic the reticular mesh of the spleen. Additional information on the microfluidic devices used in this experiment can be found in the Supplementary Material and in ref [9].

A schematic view of the chip and a focus on the portion between the barrier and the pillars are shown in Fig. 2.

## 2.1 RBCs perfusion

The Precision Pressure Control System (P2CS, Biophysical Tools GMBH) was used to regulate the flow pressure in the microfluidic device. The pump and microfluidic chip were connected by a 1 mm flexible plastic tubing (Tygon) at the inlet hole. A constant pressure of 150-200 mbar was applied at room temperature.

## 2.2 Artificial video generation

To verify the capability of the platform to detect the lack of plasticity in RBCs under rotations in the 3D environment, we generated simulated video sequences containing a deformed/rotated artificial RBC (see some examples in Fig. 3 panel A).

## 1.3 Red Blood Cell Mathematical Description

To generate the phantom images containing an RBC under deformation, we have first modelized an undeformed RBC as a surface in the 3D (x,y,z) Cartesian space, using the following formula:

$$z = \pm D_0 \sqrt{1 - \frac{4(x^2 + y^2)}{D_0^2}} \left[ a_0 + a_1 \frac{(x^2 + y^2)}{D_0^2} + a_2 \frac{(x^2 + y^2)^2}{D_0^4} \right] \quad (1)$$

where $D_0$ represents the mean diameter of the cell, $a_0$, $a_1$, and $a_2$ represent shape factors obtained during the 2D nonlinear fitting. In particular, the quantity $D_0 a_0$ represents the minimum thickness of the biconcave model at the center of the cell, whilst $a_1$ and $a_2$ regulate the convexity and relate to the maximum thickness of the disc. Values $D_0 = 7.82\ \mu m$, $a_0 = 0.052, a_1 = 2.003$ and $a_2 = -4.491$ were set according to the literature [44,45,46].

### 1.3.1 Deformation model

Let us denote with $x$ the direction along which the fluid drags the RBC and with $y$ the orthogonal direction (i.e., that of constriction). We also assume that the cell is not rotated when it passes through the constriction because of the short height of the channel and the

imposed laminar flow condition. This hypothesis has been qualitatively verified in the real image analysis section.

When the RBC passes through a constriction, it squeezes along the $y$-axis. Since the cell quickly goes beyond the obstacle, due to the local increase of fluid velocity, we can assume that the same amount of longitudinal strain $\varepsilon_l = \varepsilon_y = \frac{\Delta y}{y}$ is applied to every part of the cell. With this assumption, we can calculate $\varepsilon_l$ by imposing that the RBC's diameter (7.82 $\mu m$) is reduced to the minimum distance between the constrictions (1.5 $\mu m$) only along the $y$-axis.

Under an assumption of incompressibility of RBC [47, 48], the Poisson ratio $of\ RBC$ is calculated to be equal to 0.5. Given the magnitude of $\nu$, we can calculate the transverse strain $\varepsilon_t = \varepsilon_x = \varepsilon_z$ by multiplying the longitudinal strain by the Poisson ratio.

Once the strain is applied, the viscoelastic properties of the RBC avoid the cell restoring its initial state immediately. To describe this phenomenon, we have used the Kelvin-Voigt model [49, 50]. By applying that model to our case study, it resulted in an exponential strain relaxation model, characterized by a time constant $\tau$, which depended on the health condition of the cell [44] as follows:

$$\varepsilon(t) = \varepsilon_0 e^{-(t-t_0)/\tau} \qquad (2)$$

$\varepsilon_0$ is the initial strain applied by the funnel in a given direction and $t_0$ is the relaxation starting time. In our study, the latter is always set to zero. The values of $\tau$ are randomly generated from two distinct Gaussian populations with average values equal to 25 (σ = 5) and 8 (σ = 2) for unhealthy and healthy conditions, respectively (see Fig. 3 panel B). Mean and variance of the time constant $\tau$ are extrapolated by a first analysis of the acquired videos. As expected, we used a lower $\tau$ average value for healthy RBCs to simulate their ability to restore their original shape faster. On the contrary, a higher $\tau$ average value represented a slower restoring of the original shape, therefore lower plasticity. The higher the standard deviation simulated, the higher the morphology heterogeneity of the unhealthy cells. During its relaxation time, the cell could be subjected to external forces that could alter the initial orientation of the cell. The forces are essentially due to the non-uniformity flux given by the numerous constrictions, to the interaction with the other cells, and, especially, to a slightly uneven application of stress by the constriction. However,

under the quasi-planar assumption and the progressive levelling out of the flux velocity, the angle oscillations are bounded in a reduced range.

To simulate this effect, we have rotated the deformed geometry at a certain time after the stress application using specific rotation matrices. Mathematical details of the rotation matrices can be found in the Supplementary Material.

## 2.3 Real dataset

### 2.3.1 Time-lapse Microscopy video acquisition

Videos sequences were made up of around 1000 frames with a camera speed of 85 fps. Before recording the videos, RBCs were pumped for 1 minute to stabilize the microfluidic unit conditions. Optical measurements were performed using a microscope (Zeiss) and Zeiss Axiocam 503 mono camera. While RBCs were perfused through the chip, several videos were recorded for analysis. A total of 54 videos were collected (41 videos from healthy donors and 13 from PKD subjects).

### 2.3.2 Data processing

The data processing step is composed of several blocks (Fig. 1 B)-G)) aimed at preprocessing the video sequence, localizing and tracking objects of interest (RBCs), and extracting that information relevant for the automatic recognition of pathological cell behavior with respect to the source of deformation induced by pillars, i.e., the so-called lack of plasticity of cells.

*i) Video Processing*

Each frame is cropped in order to confine the analysis in the region between the barrier and pillars (Fig. 1 panel B). To eliminate pillars from the frame, we applied an *inpainting* procedure [51, 52] with the aim of restoring the targeted regions in a given image using neighboring information. Pillars are located by using the Circular Hough Transform (CHT) [53] with radius tolerance [10-20] px and a sensitivity parameter value equal to 0.90. The circular regions corresponding to the six pillars are then used as targeted regions for inpainting, as shown in the right picture in the video processing step (panel B Fig. 1), where pillars have been removed from the image.

*ii) Cell localization and tracking*

Each frame is then processed again using the CHT with radius tolerance (4-10) px tuned according to a manual estimation of the diameter of the RBC. RBCs located at each frame are then processed using a modified version of proprietary cell-tracking software, i.e., Cell Hunter [6,7,54] (Fig. 1 panel C). The modifications introduced here are related to the flow direction constraint over the set of linkable cells in the assignment matrix. In this work, we limit the instantaneous turning angle [55] of the trajectory in the range $[-\pi/6, \pi/6]$. Thanks to this, the method is robust to cell velocity variability or to cell density increasing that is slightly observed during the experiment.

*iii) ROI Sequence (ROI-S) extraction and equalization*

In order to finely characterize the morphology of each RBC during its motion in the chip, the algorithm extracts a Region Of Interest (ROI) around the located cells for each time point, therefore generating what we call ROI sequence (ROI-S). To avoid the introduction of heterogeneity in luminance from one frame and another, we applied an adaptive histogram equalization procedure [54] by improving the contrast in the first frame using histogram stretching techniques and using histogram matching procedures [56] to gradually adapt the contrast of the frames to the first one. An example of equalized ROI-S is shown in Fig.1 panel D, where an RBC slowly passes from a circular shape to an oblong shape while approaching the pillars. As it can be noted, the ROI-S still maintains the overall original appearance and the general contrast appears uniform along the sequence.

*iv) Filtered ROI-S extraction*

To account for the confounding effect of background illumination, we extracted the derivative of each ROI-S along the two dimensions by progressively applying the Laplacian of Gaussian (LoG) [56] filter in each frame. In this way, only the shape of the cell is highlighted to characterize the changes in shape during the video sequence. An example of the LoG filtered ROI-S is shown in Fig.1, panel E. Mathematical details of the LoG filter used can be found in the Supplementary Material. As it can be seen, the differential sequence contains only the information related to parts of the cells, thus reducing the effect of background conditions. It is important to note that this step is relevant regardless of the fact

that cells move, but is crucial for any TLM application involving morphological cell characterization.

*v) Deep Learning differential ROI-S encoding*

Transfer-learning represents an alternative to solve the problem of insufficient labeled training data in deep learning architecture [57-60]. Among various transfer learning strategies [61], we focus our attention on the so-called deep network-based transfer learning, in which the front layers of the network can be treated as a feature extractor, and the extracted features are versatile. More specifically, in [60], the authors demonstrated that pre-trained networks such as AlexNet [62] and ResNet-101 [63] are good choices in deep transfer learning based on networks. To expand the plethora of networks for transfer learning purposes, we also compared the recently added NASNetLarge [64] network. For each network, we resized the differential ROI-S frames to specific dimensions (see Table I) and selected a specific layer for feature extraction. To adapt the frame size to the requested dimension, we used a bilinear interpolation technique. From the observation of the network's characteristics, it resulted that the number of features extracted may be very different for each network.

*vi) Cooperative classification*

The extracted features are subjected to a feature selection procedure based on the individual ability to discriminate PKD and healthy RBCs in a validation set extracted for the scope of the artificial and real datasets. A restricted number of features is then used in a standard classification task by means of Linear Discriminant Analysis (LDA) [53]. As indicated in Fig. 1 (panels F and G), a label is generated for each frame along the trajectory of a single cell (see the sequence of green and red bars). In order to account for confounding phenomena, i.e., projection of 3D shape over a 2D domain, dis-uniformity of PKD cells that may not be affected in the same manner by the disease, and lastly, not less relevant, the path of each individual cell that may be not subjected to deformation, we designed a decision-making strategy based on cooperative learning. In particular, we applied two distinct decision strategies: at the track level and at the experiment level (used only for the real dataset). In a first step, the software evaluates the percentage of positive frames along the same track, and secondly, it evaluates the percentage of positive tracks in the same experiment. Such

percentages are compared with the threshold. In this way, the platform may act in a more or a less conservative attitude by switching to higher sensitivity (we accepted false positives but not false negatives, high recall rate, low precision) or to higher specificity (we preferred false negatives to false positives, high precision, low recall rate). The two-threshold strategy was inspired by the standard protocol to assess a final diagnosis by using a pipeline of subtasks (e.g., if a given number of clinical tests resulted in positives, then the subject is assigned a certain diagnosis).

*vii) Statistical analysis*

With the aim to demonstrate the effectiveness of the proposed platform, we considered here 54 experiments, 13 related to PKD and 41 to healthy RBCs (see Results section). A leave-one-experiment-out cross-validation strategy was used for the scope of evaluating the classification accuracy. The results were summarized in terms of balanced classification accuracy (ACC), that is, the average value of sensitivity (true positive rate) and specificity (true negative rate). The effect of the selection of the threshold values $th_1$ and $th_2$ were also investigated by exhaustive analysis over a reasonable range of values.

### 2.4 Detection of lack of deformability in artificial frames

To apply the platform to the simulated experiments, we artificially generated 50K frames containing an artificially rotated/deformed RBC. A general idea of the simulated experiments is sketched in Fig. 3 (panels A-D). The entire frame sequences generated and the source code to generate the sequences of tracks can be found at the following link: https://cloudstore.bee.uniroma2.it/index.php/s/8NnRRn2ZeFpDzG9, PW: RBC2_SAA

#### 2.4.1 Images generation

Once the surface representing the RBC is described, deformed, and rotated by a triplet of angles, generated randomly by a normal distribution with zero mean and 30° variance (thus letting the surface be rotated mainly for small angles), a track of 50 images from the top view is generated. By repeating the procedure, we generated approximately 500 tracks for each condition (healthy and unhealthy), thus leading to about 50K frames in total. Fig. 3 Panel A shows some examples of RBCs generated with different rotation angles and degrees of deformability. Fig. 3 Panel B shows the two distributions used for the two classes of RBC.

2.4.2 Image sequence analysis

The platform for the analysis described in Section 2 is applied with slight modifications to the artificial images. In particular, only steps (E)-(G) in Fig. 1 are applied due to the fact that cell localization and tracking are intrinsically already available after video sequence generation. Therefore, first, the differential ROI-S is calculated (step E Fig. 1) to make the system robust to general luminance conditions. Then, each ROI-S is passed in input to the deep learning algorithm and coded into deep features (step F Fig. 1). Provided a classification label at a single frame level for each ROI-S, a single-threshold strategy is here applied (only $th_1$) since we did not simulate any inter-experiment heterogeneity to motivate the use of a second threshold value.

2.4.3 Classification in artificial images

Fig. 3 Panel C shows the distribution of the classification errors at frame level (false positives and false negatives, that is, healthy RBC assigned to unhealthy and unhealthy RBC assigned to the healthy class) with respect to the timing of the errors. As it can be noted, most of the false positive frames occur at the beginning of the track of healthy cells in the presence of very big rotation angles. On the contrary, most false negatives occur at the end of the path of unhealthy cells when a too-small value has been used for unhealthy RBCs. Anywhere, Fig. 3 Panel D shows that the use of the majority voting procedure at the track level allows compensating such errors when the percentage of the positives frames exceeds a threshold value (the majority corresponds to using a threshold value equal to 0.5).

Figure 4 shows the accuracy matrices obtained after the analysis of the artificial images. From left to right, results at the single frame level using a majority voting procedure (threshold value on the percentage of positive instances equal to 0.5), thresholding result with adaptive threshold optimized in a validation subset of frames.

## *3. Results*

Hereby, we present numerical results from the real case study for the classification of PKD versus healthy RBC cells using the described platform.

3.1 Cell frames and tracks analyzed

Due to the long-time experiments and the fast camera, a very high number of cell tracks were analyzed. In particular, we acquired 54 experiments (13 from PKD and 41 from healthy donors) for a total number of 135631 single cell frames (55457 for PKD and 80174 for healthy). A total number of 3236 tracks were analyzed, out of which 1408 came from PKD and 1828 from healthy donors. The huge number of data analyzed is a further demonstration of the reliability of the proposed platform.

3.2 ROI differentiation (LoG ROI-S) to improve deep-feature discrimination capability

Deep-transfer learning has enormous potential to avoid retraining the network and the consequent need to acquire a large dataset for the retraining step. On the other hand, it is crucial that the features extracted in this way are totally robust to a change in luminance to avoid the introduction of a bias that may impair the classification results. In light of this, one of the key aspects of the proposed platform is the differentiation step of the ROI sequence by means of LoG filtering. To demonstrate the effectiveness of such a procedure over the discrimination capabilities of the deep features extracted for the task of classification, we performed a specific simulation. For all 3K tracks considered in the experiments, we applied a brightening/darkening procedure by randomly summing a luminance level in the uniform range [-0.5, 0.5] to the entire ROI-S (negative values indicate darkening and positive values indicate brightening) where 0 indicates no degradation. Such kind of setting is related to the fact that thanks to the sequence equalization procedure applied, we may always balance the luminance among frames in the same sequence. We then compare the discriminative capability of deep features extracted over the modified sequences of frames without differentiation (i.e., standard ROI-S) and with the application of LoG filtering (i.e., LoG ROI-S). To evaluate the discriminative power of the 30 most significant deep features extracted using the AlexNet network, we computed the so-called Discriminant Power (DP) index defined as

$$DP = \max(1 - AUC, AUC) \quad (5)$$

where AUC is the Area Under the roC curve [62] of each individual feature. Being AUC in the range [0, 1], DP is in the range [0.5, 1], where 0.5 indicates no capability to discriminate and one denotes perfect capability. Figures 5 (A)-(B) illustrate for any level of degradation in the range [-0.5, 0.5] the maps of the corresponding DP for the 30 features. The colorbar is

also indicated. It can be noted that the discrimination capabilities of deep features using the LoG filters operation (A) are remarkably higher than those obtained using the standard mode (B). Moreover, it can also be observed that, as expected, deep features are influenced by brightening/darkening, since the maximum performances are achieved when the level of degradation is zero. However, as also shown in the boxplot in panel C of Fig.5, the worsening of the DP values in relation to the degradation level is much more limited in the LoG ROI-S condition than in the standard mode.

This simulation not only confirmed the high values of DP for the extracted features but also demonstrated the importance of performing the preprocessing of the ROI-S to limit the effect of unpredictable degradation processes occurring during the experimental session when using deep transfer learning in dynamical system investigation.

### 3.3 Visual cue of deep features

Deep features were extracted by the inner layer of a given pretrained CNN architecture. The nonlinear high complex network structure makes it so difficult to have a direct understanding of which image portion features represent. On the other hand, it could be very informative to have at least a visual cue of the feature maps selected for the task of classification. To do this, we extract for two different ROI-S the corresponding feature maps extracted at layer 'pool5' of AlexNet CNN for those features that exhibited higher discriminative capabilities in terms of DP (Eq. 5). Figure 6 shows two examples of sequences of feature maps of two LoG ROI-S in which the RBC changes shape during motion.

It is interesting to note that the most activated features in these maps correspond to the most deformed shapes. This evidence supported the assumptions that the selected features were sensitive to cell morphology and shape deformation and, therefore, were more suitable to discriminate pathological from physiological lack of plasticity.

### 3.4 Best classification performance of comparative deep learning networks

We compared the classification results obtained by exploiting three distinct deep learning neural networks for transfer learning. By optimizing the threshold values, $th_1$ and $th_2$, we obtained the best performance listed in Table II in terms of ACC values at a single frame level without thresholding (first column), using a single threshold setting computed over the percentage of positive frames over the entire video (second column), and using the two

threshold strategy (third column), one for the positive frames in each track ($th_1$) and one for the positive tracks in each video ($th_2$). As it can be seen, the networks achieved almost very similar results demonstrating the robustness of the approach and the acceptable independence of the networks from the data.

In addition, despite its old dating, it is also evident that AlexNet, as elsewhere demonstrated [65], is one of the top approaches for transfer learning, exhibiting a high capability of image encoding. The reduced number of layers and consequently the simpler network architecture of AlexNet make it the optimal solution for our approach, representing an acceptable trade-off between complexity and accuracy.

### 3.5 Multi-threshold decision-making strategy results

To demonstrate the effect of varying threshold values in the cooperative strategy of two thresholds, we computed the ACC metric for any combination of threshold values in a predetermined range [0.2, 0.6]. This range has been selected to avoid limited conditions occurring. Figure 7 shows the ACC results for different combinations of the threshold values for the three networks.

As demonstrated by the three maps, accuracy values are very high for a large set of threshold combinations, especially for AlexNet and NasNetlarge architecture. This finding again proves the reliability of the approach as well as the robustness to different network architectures.

## *4. Discussion and further developments*

Techniques available for the study of plasticity force cell deformation of RBCs using strong stress, such as that provided by the barrier, and thus emulating the travel through capillaries. Traditional bulk flow, single-cell deformability measurements, and microfluidics devices-based platforms standardly present experimental scenarios based on the working principle of measuring the stress induced by some form of force in order to quantitatively evaluate the deformability capability of each cell [9,25]. However, this implies the use of a pump and inflow modalities that may alter the physiological movement of cells resulting in being invasive and costly. In this case, information extracted through

quantitative assessment is at risk of being related to the overall experimental conditions rather than to the individual cell motility morphodynamic aspects.

To reduce this variability and confer more stability and uniformity on the experiments carried out in this context, we proposed some solutions.

To demonstrate the capability of the proposed platform to discriminate the lack of plasticity in PKD cells from healthy RBCs also under rotations in the environment, we preliminarily presented simulation results by generating artificial frames of 3D rotated/deformed RBCs with different degrees of plasticity, also with the aim of stressing the device working principle.

In the real scenario, we focused the analysis on the deformation-induced under non-stress conditions, such as that provided by the forest of pillars zoomed in Fig. 2 panel C and the prepared carrier solution. In this case, cells physiologically moved towards pillars and deformed to overcome the obstacles.

In addition, to reduce the influence of the environmental condition (optical properties of the medium and of the material used for the chip) on the video and ML analysis, we applied a specific preprocessing to the acquired video sequence. In particular, after trajectories were extracted, we reformulated the analysis on the differential sequence of ROIs, LoG ROI-S, extracted around the cell track in order to reduce the influence of change in illumination over the discrimination capability of the deep features extracted.

Third, by exploiting ML cooperative decision strategies, inspired by a blind multi-expert clinical evaluation procedure, we implemented a two-level decision-making procedure: a single track (namely a single ROI-S) was assigned a unique label by comparing the percentage of frames assigned to the positive class at single frame level with a given threshold, $th_1$. The same procedure was then applied at the experiment level, using the threshold $th_2$. In this way, the platform acted as a team supervisor who had the task of assigning a diagnosis to the patient after collecting the independent opinions of his/her collaborators. Such a paradigm allowed modulating the recall and the precision rate for a given task, moving from screening to diagnostic purposes (i.e., high sensitivity vs high specificity).

The main assumption behind such a procedure is that the evidence of a single RBC disease may be obscured by its movement (rigid rotation instead of deformation) and by acquisition conditions (spatial resolution, frame rate). Moreover, it is expected that along with the movement, the cell presents an oblong shape only in some frames, passing from being round shaped to elongated and back to round shaped. On the other hand, if the percentage of frames in which the cell is visualized and assigned a positive label is sufficiently high, then we may conclude that the cell track is labeled as positive. The same reasoning is applied at the experiment level.

The presented modifications go in the direction of improving the generalizability of the platform for the analysis of deformability, allowing the consideration of many different sources of influence that can be encountered in real applications [25]. The joint action of microfluidics, low-cost video analysis, and robust machine learning techniques gives the platform robustness to the calibration transfer problem and the possibility of readjustment to different diagnostic scenarios (other cell types, other diseases, presence of external stimuli).

## *5. Conclusions*

We present here a novel platform for the biological investigation of ex-vivo experiments called machine learning microfluidics. Thanks to the fruitful cooperation of artificial intelligence and microfluidic devices, the platform is able to capture the cell morphodynamic aspects during its motion in a preconfigured environment. In this regard, to demonstrate the relevance of the proposed solutions designed, we simulated a scenario with generated RBCs framed under different 3D rotations/deformation conditions and verified the capability of the platform to discriminate RBCs with lack of plasticity from healthy RBCs in critical scenarios. Then, we validated the platform in the identification of RBCs Pyruvate Kinase Disease (PKD), highlighting very high classification results. Future works will expand the present approach in new directions. First, cell morphology and related temporal variation could be studied using time-varying deep features and related cross-dependencies. Finally, and not less relevant, the same platform would also be used for drug testing in relation to the effect of treatment on cell phenotyping or to identify and/or diagnose different diseases that affect the membrane integrity of the RBC.

## *6. Acknowledgments*

The authors would like to thank Miguel A. Martin for the careful maintenance of PKD deficient mice, and Ms Isabel Ojeda-Perez for her help in blood extraction. This work was supported by grants from "Ministerio de Economía, Comercio y Competitividad y Fondo Europeo de Desarrollo Regional (FEDER)" (SAF2017-84248-P), "Fondo de Investigaciones Sanitarias, Instituto de Salud Carlos III" (Red TERCEL; RD16/0011/0011 and Networking Biomedical Reserach Center (CIBER) CIBER is an initiative funded by the National R&D&i Plan 2008–2011, Iniciativa Ingenio 2010, Consolider Program, CIBER Actions, and the Instituto de Salud Carlos III (RD16/0006/0012) and Comunidad de Madrid (AvanCell, B2017/BMD-3692). The authors also thank Fundación Botín for promoting translational research at the Hematopoietic Innovative Therapies Division of the CIEMAT. CIBERER is an initiative of the "Instituto de Salud Carlos III" and "Fondo Europeo de Desarrollo Regional (FEDER)". The authors want to acknowledge MicroFabSpace and Microscopy Characterization Facility, Uni of ICTS "NANBIOSIS" from CIBER-BBN at IBEC. This work was funded by the European Commission H2020-MSCA-ITN-2019, Grant Agreement N860436, "EVIDENCE" and by the CERCA Programme and by the Commission for Universities and Research of the Department of Innovation, Universities, and Enterprise of the Generalitat de Catalunya (2017 SGR 1079), it has been developed in the context of AdvanceCat with the support of ACCIÓ (Catalonia) Trade and Investment; Generalitat de Catalunya) under the Catalonian ERDF operational program (European Regional Development Fund) 2014–2020.

**References**


[1] Bhatia, Sangeeta N., and Donald E. Ingber. "Microfluidic organs-on-chips." Nature Biotechnology 32.8 (2014): 760-772.

[2] Azizipour, Neda, et al. "Evolution of biochip technology: A review from lab-on-a-chip to organ-on-a-chip." Micromachines 11.6 (2020): 599.

[3] Jeong, Sehoon, et al. "A three-dimensional arrayed microfluidic blood–brain barrier model with integrated electrical sensor array." IEEE Transactions on Biomedical Engineering 65.2 (2017): 431-439.

[4] Thompson, Alex J., et al. "Design analysis and optimization of a single-layer PDMS microfluidic artificial lung." IEEE Transactions on Biomedical Engineering 66.4 (2018): 1082-1093.

[5] Samiei, Ehsan, et al. "Investigating Programmed Cell Death and Tumor Invasion in a Three-Dimensional (3D) Microfluidic Model of Glioblastoma." International journal of molecular sciences 21.9 (2020): 3162.

[6] Nguyen, Marie, et al. "Dissecting effects of anti-cancer drugs and cancer-associated fibroblasts by on-chip reconstitution of immunocompetent tumor microenvironments." Cell Reports 25.13 (2018): 3884-3893.

[7] Di Giuseppe, Davide, et al. "Learning cancer-related drug efficacy exploiting consensus in coordinated motility within cell clusters." IEEE Transactions on Biomedical Engineering 66.10 (2019): 2882-2888.

[8] Mencattini, Arianna, et al. "A microfluidic device for shape measurement in red blood cells (RBCs)." 2020 IEEE International Symposium on Medical Measurements and Applications (MeMeA). IEEE, 2020.

[9] Rizzuto, V., Mencattini, A., Álvarez-González, B., Di Giuseppe, D., Martinelli, E., Beneitez-Pastor, D., ... & Samitier, J. (2021). Combining microfluidics with machine learning algorithms for RBC classification in rare hereditary hemolytic anemia. Scientific Reports, 11(1), 1-12.

[10] Van den Broek, Lenie J., et al. "Progress and future prospectives in skin-on-chip development with emphasis on the use of different cell types and technical challenges." Stem Cell Reviews and Reports 13.3 (2017): 418-429.

[11] Routy, Bertrand, et al. "Gut microbiome influences efficacy of PD-1–based immunotherapy against epithelial tumors." Science 359.6371 (2018): 91-97.

[12] Ongaro, Alfredo E., et al. "Polylactic is a sustainable, low absorption, low autofluorescence alternative to other plastics for microfluidic and organ-on-chip applications." Analytical Chemistry 92.9 (2020): 6693-6701.

[13] Osaki, Tatsuya, et al. "In vitro microfluidic models for neurodegenerative disorders." Advanced Healthcare Materials 7.2 (2018): 1700489.

[14] Comes, M. C., et al. "The influence of spatial and temporal resolutions on the analysis of cell-cell interaction: a systematic study for time-lapse microscopy applications." Scientific Reports 9.1 (2019): 1-11.

[15] Mencattini, A., et al. "Discovering the hidden messages within cell trajectories using a deep learning approach for in vitro evaluation of cancer drug treatments." Scientific Reports 10.1 (2020): 1-11.

[16] Xu, Liyi, et al. "Virtual microfluidics for digital quantification and single-cell sequencing." Nature Methods 13.9 (2016): 759-762.

[17] Eulenberg, P., et al., (2017). "Reconstructing cell cycle and disease progression using deep learning." Nature Communications, 8(1), 1-6.

[18] Damiati, Samar, et al. "Microfluidic devices for drug delivery systems and drug screening." Genes 9.2 (2018): 103.

[19] Parlato, Stefania, et al. "3D Microfluidic model for evaluating immunotherapy efficacy by tracking dendritic cell behaviour toward tumor cells." Scientific Reports 7.1 (2017): 1-16.

[20] Goudar, V. S., Yeh, P. H., Wu, S. Y., Chu, C. H., Lu, L. S., Yang, C. H., ... & Tseng, F. G. (2020). Live circulating tumour cells selection on digitized self-assembled cell array (Digi-saca) chip by in-parallel/in-situ image analysis, cell capture, and cultivation. Sensors and Actuators B: Chemical, 316, 128002.

[21] Badiola-Mateos, M., Di Giuseppe, D., Paoli, R., López, M. J., Mencattini, A., Samitier, J., & Martinelli, E. (2021). A novel multi-frequency trans-endothelial electrical resistance (MTEER) sensor array to monitor Blood-Brain Barrier integrity. Sensors and Actuators B: Chemical, 129599.

[22] Iragorri, Maria Alejandra Lizarralde, et al. "A microfluidic approach to study the effect of mechanical stress on erythrocytes in sickle cell disease." Lab on a Chip 18.19 (2018): 2975-2984.

[23] Lin, Jin-Young, et al., "A microfluidics-based wound-healing assay for studying the effects of shear stresses, wound widths, and chemicals on the wound-healing process." Scientific Reports 9.1 (2019): 1-11.

[24] Duffy DC, et al., "Rapid Prototyping of Microfluidic Systems in Poly(dimethylsiloxane)." Anal Chem 1998;70:4974-84

[25] Matthews, K., Lamoureux, E. S., Myrand-Lapierre, M. E., Duffy, S. P., & Ma, H. (2022). Technologies for measuring red blood cell deformability. Lab on a Chip.

[26] Islamzada, E., Matthews, K., Lamoureux, E., Duffy, S. P., Scott, M. D., & Ma, H. (2022). Blood unit segments accurately represent the biophysical properties of red blood cells in blood bags but not hemolysis. Transfusion, 62(2), 448-456.

[27] Besedina, N. A., Skverchinskaya, E. A., Ivanov, A. S., Kotlyar, K. P., Morozov, I. A., Filatov, N. A., ... & Bukatin, A. S. (2021). Microfluidic Characterization of Red Blood Cells Microcirculation under Oxidative Stress. Cells, 10(12), 3552.

[28] Lamoureux, E. S., Islamzada, E., Wiens, M. V., Matthews, K., Duffy, S. P., & Ma, H. (2022). Assessing red blood cell deformability from microscopy images using deep learning. Lab on a Chip, 22(1), 26-39.

[29] Zanella A, Fermo E, Bianchi P, Valentini G. Red cell pyruvate kinase deficiency: molecular and clinical aspects. Br J Haematol. 2005 Jul;130(1):11-25.

[30] Grace RF, Zanella A, Neufeld EJ, Morton DH, Eber S, Yaish H, et al. Erythrocyte pyruvate kinase deficiency: 2015 status report. American Journal of Hematology. 2015;90(9):825-30.

[31] Aizawa, S., Kohdera, U., Hiramoto, M., Kawakami, Y., Aisaki, K., Kobayashi, Y., Miwa, S., Fujii, H. & Kanno, H. (2003) Ineffective erythropoiesis in the spleen of a patient with pyruvate kinase deficiency. American Journal of Hematology, 74, 68–72.

[32] Grace, Rachael F., and Wilma Barcellini. "Management of pyruvate kinase deficiency in children and adults." Blood 136.11 (2020): 1241-1249.

[33] Radosinska J, Vrbjar N. The role of red blood cell deformability and Na,K-ATPase function in selected risk factors of cardiovascular diseases in humans: focus on hypertension, diabetes mellitus and hypercholesterolemia. Physiol Res. 2016 Sep 19;65 Suppl 1:S43-54.

[34] Gambhire, Priya, et al. "High Aspect Ratio Sub-Micrometer Channels Using Wet Etching: Application to the Dynamics of Red Blood Cell Transiting through Biomimetic Splenic Slits." Small 13.32 (2017): 1700967.

[35] Gallagher, Patrick G., and Bertil Glader. "Diagnosis of pyruvate kinase deficiency." Pediatric Blood & Cancer 5.63 (2016): 771-772.

[36] Mehri, R et al., "Red Blood Cell Aggregates and Their Effect on Non-Newtonian Blood Viscosity at Low Hematocrit in a Two-Fluid Low Shear Rate Microfluidic System." PLoS One 2018, 13 (7).

[37] Iragorri, M. A. L., El Hoss, S., Brousse, V., Lefevre, S. D., Dussiot, M., Xu, T., ... & El Nemer, W. (2018). A microfluidic approach to study the effect of mechanical stress on erythrocytes in sickle cell disease. Lab on a Chip, 18(19), 2975-2984.

[38] Aurich, K et al., "Label-Free on Chip Quality Assessment of Cellular Blood Products Using Real-Time Deformability Cytometry." Lab Chip 2020, 2306–2316.

[39] Faustino, V et al., "A Microfluidic Deformability Assessment of Pathological Red Blood Cells Flowing in a Hyperbolic Converging Microchannel." Micromachines 2019, 10 (10).

[40] Picot, J. et al., "Biomimetic Microfluidic Chip to Study the Circulation and Mechanical Retention of Red Blood Cells in the Spleen." Am. J. Hematol. 2015, 90 (4), 339–345.

[41] Mao, X. and Huang, T. J. "Exploiting Mechanical Biomarkers in Microfluidics." Lab Chip 2012, 12 (20), 4006–4009.

[42] Cluitmans, J. C. A et al., "Alterations in Red Blood Cell Deformability during Storage : A Microfluidic Approach." BioMed research international 2014.

[43] Min-Oo G, Fortin A, Tam MF, Gros P, Stevenson MM. "Phenotypic expression of pyruvate kinase deficiency and protection against malaria in a mouse model." Genes Immun. 2004 May;5(3):168-75.

[44] E. Evans e Y.-C. Fung, «Improved measurements of the erythrocyte geometry.» Microvascular Research, 1972.

[45] D. Yoon e D. You, «Continuum modeling of deformation and aggregation of red blood cells,» Journal of Biomechanics, 2015.

[46] X. Qi, S. Wang, S. M, K. Han e X. Li, «Quantitative prediction of flow dynamics and mechanical retention of surface-altered red blood cells through a splenic slit,» Physics of Fluids, 2021.

[47] K.-i. Tsubota, «Elongation deformation of a red blood cell under shear flow as stretch testing,» Journal of the Mechanics and Physics of Solids, 2021.

[48] M. T.Eraky, A. I. El-Rahman, M. H.Shazly e M. M.Abdelrahman, «Mechanics of deformation of malaria-infected red blood cells,» Mechanics Research Communications, 2021.

[49] R. Przekop, I. Majewski e A. Moskal, «Modelling of erythrocyte behaviour in blood capillaries by structural model combined with lattice-boltzmann approach,» Chemical and Process Engineering, 2018.

[50] J. E. Mancuso e W. D. Ristenpart, «Stretching of red blood cells at high strain rates,» Phys. Rev. Fluids, 2017.

[51] Criminisi, A., et al., "Region Filling and Object Removal by Exemplar-Based Image Inpainting." IEEE Transactions on Image Processing. Vol. 13, No. 9, 2004, pp. 1200–1212.

[52] Le Meur, et al., "Hierarchical Super-Resolution-Based-Inpainting." IEEE Transactions on Image Processing. Vol. 22, No. 10, 2013, pp. 3779–3790.

[53] E.R. Davies, Machine Vision: Theory, Algorithms, Practicalities. Chapter 10. 3rd Edition. Morgan Kauffman Publishers, 2005.

[54] Munkres, J., 1957. "Algorithms for the assignment and transportation problems." Journal of the society for industrial and applied mathematics 5, 32–38.

[55] Gorelik, Roman, and Alexis Gautreau. "Quantitative and unbiased analysis of directional persistence in cell migration." Nature Protocols 9.8 (2014): 1931.

[56] Gonzalez, Rafael C., Richard Eugene Woods, and Steven L. Eddins. Digital image processing using MATLAB. Pearson Education India, 2004.

[57] Tan, Chuanqi, et al. "A survey on deep transfer learning." International conference on artificial neural networks. Springer, Cham, 2018.

[58] Kang, R., Park, B., Eady, M., Ouyang, Q., & Chen, K. (2020). Single-cell classification of foodborne pathogens using hyperspectral microscope imaging coupled with deep learning frameworks. Sensors and Actuators B: Chemical, 309, 127789.

[59] Gamboa, J. C. R., da Silva, A. J., & Araujo, I. C. (2021). Validation of the rapid detection approach for enhancing the electronic nose systems performance, using different deep learning models and support vector machines. Sensors and Actuators B: Chemical, 327, 128921.

[60] Yosinski, J., et al., "How transferable are features in deep neural networks?" In: Advances in Neural Information Processing Systems, pp. 3320–3328 (2014).

[61] A. Krizhevsky, et al., "ImageNet Classification with Deep Convolutional Neural Networks", NIPS Proc. (2012).

[62] He, Kaiming, et al.,. "Deep residual learning for image recognition." In Proceedings of the IEEE conference on computer vision and pattern recognition, pp. 770-778. 2016.

[63] Zoph, B., et al. (2018). “Learning transferable architectures for scalable image recognition.” In Proceedings of the IEEE conference on computer vision and pattern recognition (pp. 8697-8710).

[64] Faraggi, David, and Benjamin Reiser. "Estimation of the area under the ROC curve." Statistics in Medicine 21.20 (2002): 3093-3106.

[65] M.D. Zeiler and R. Fergus, “Visualizing and Understanding Convolutional Networks”, Eur. Conf. Comput. Vis. 12 (2014) 818–833.

*Figure 1:*

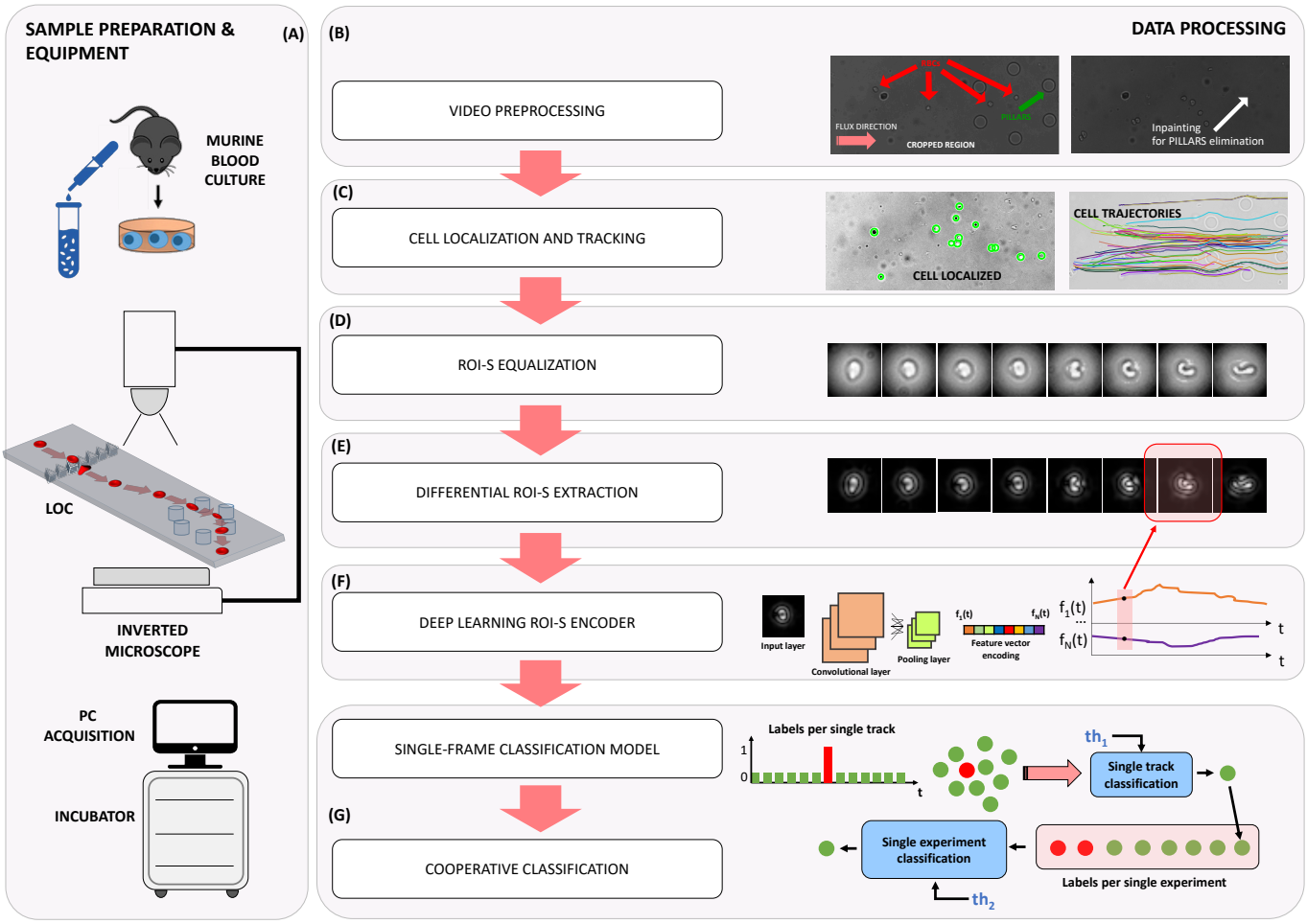


*Fig 1. A sketch of the MLM platform proposed for the RBC plasticity analysis. Panel A. Sample preparation and equipment description. Panel B. Data processing steps for video analysis and machine learning classification.*

***Figure2:***

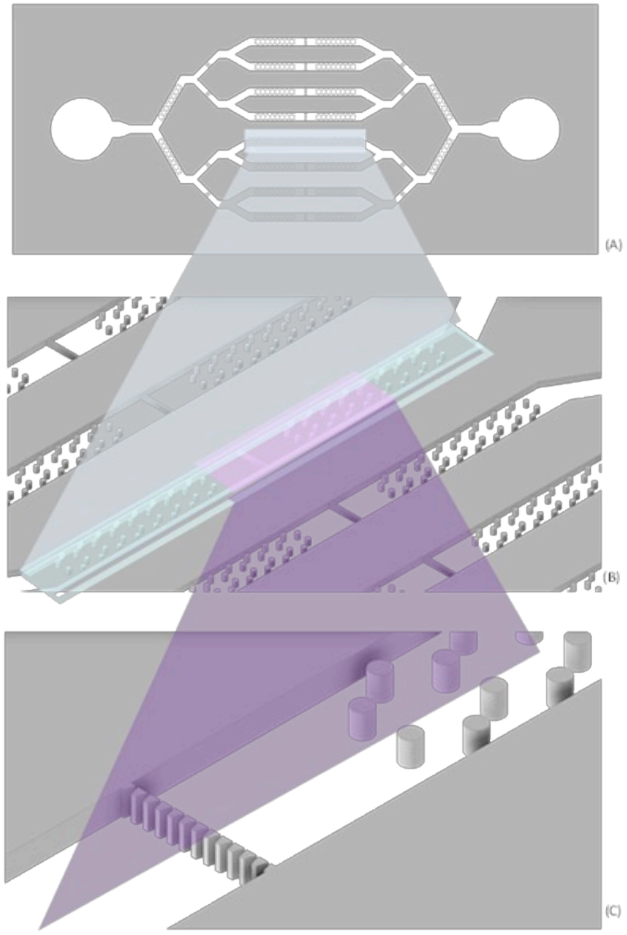


*Fig 2. A schematic layout of the chip used for the in-flow measurement. (A) top view. (B) A zoom of the microchannels and the barriers. (C) A zoom of the pillars (top-right) and barrier (bottom-left) in the channel.*

*Figure 3:*

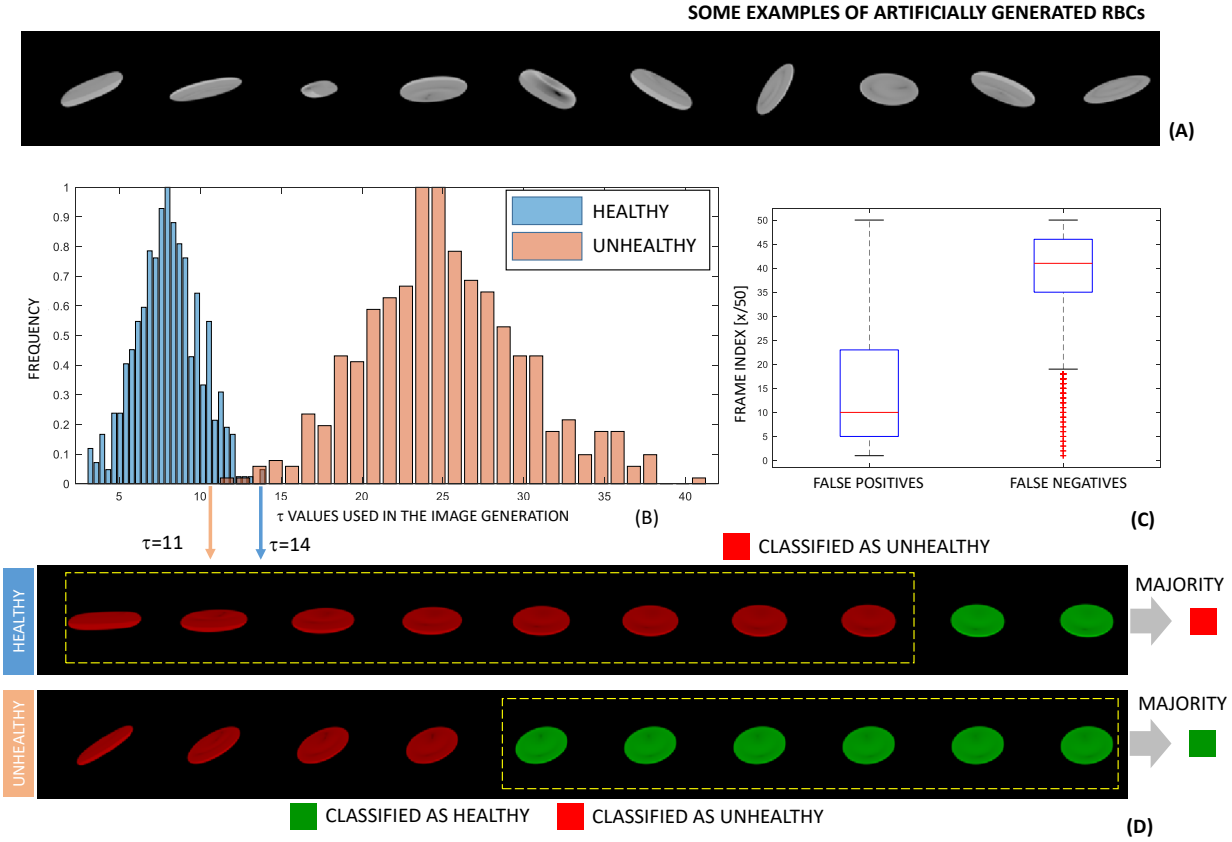


*Fig 3 A sketch of the RBC plasticity analysis in simulated experiments. (A) Some examples of rotated and deformed RBCs. (B) Distribution of the time constant $\tau$ used to simulate the different level of plasticity (blue healthy, red unhealthy). (C) Timing distribution of the two kinds of classification errors (false positives, i.e., healthy classified as unhealthy, and false negatives, i.e., unhealthy classified as healthy). (D) Two examples of healthy (upper) and unhealthy (lower) simulated RBC sequences along with the assigned class (red, unhealthy, green healthy). To the right the final class assigned by the majority voting.*

## *Figure 4*

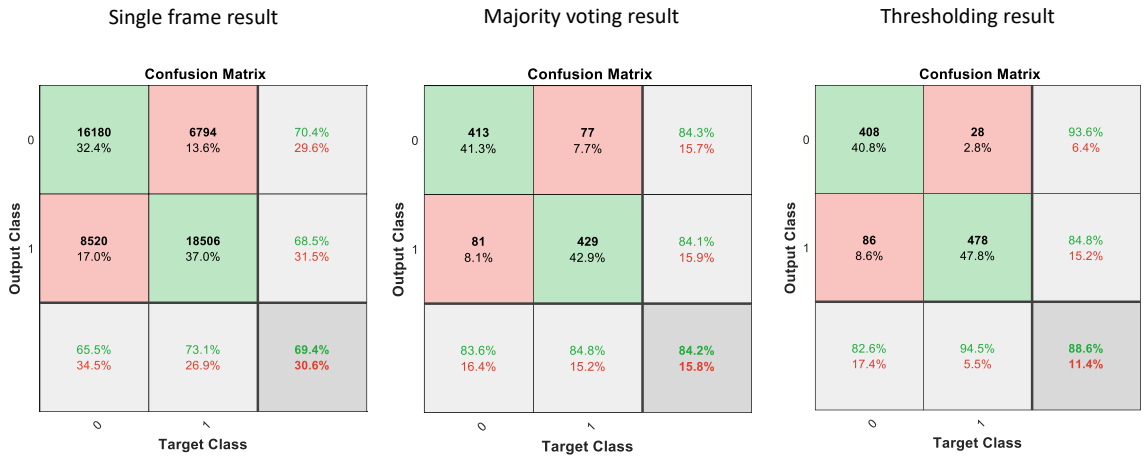


*Fig 4. Accuracy matrices for the artificial experiments. From left to right. Results at single frame level, results after majority voting (equivalent to use a threshold value over the percentage of positive instances equal to 0.5), and adaptive thresholding with optimization performed over a validation subset of images.*

*Figure 5:*

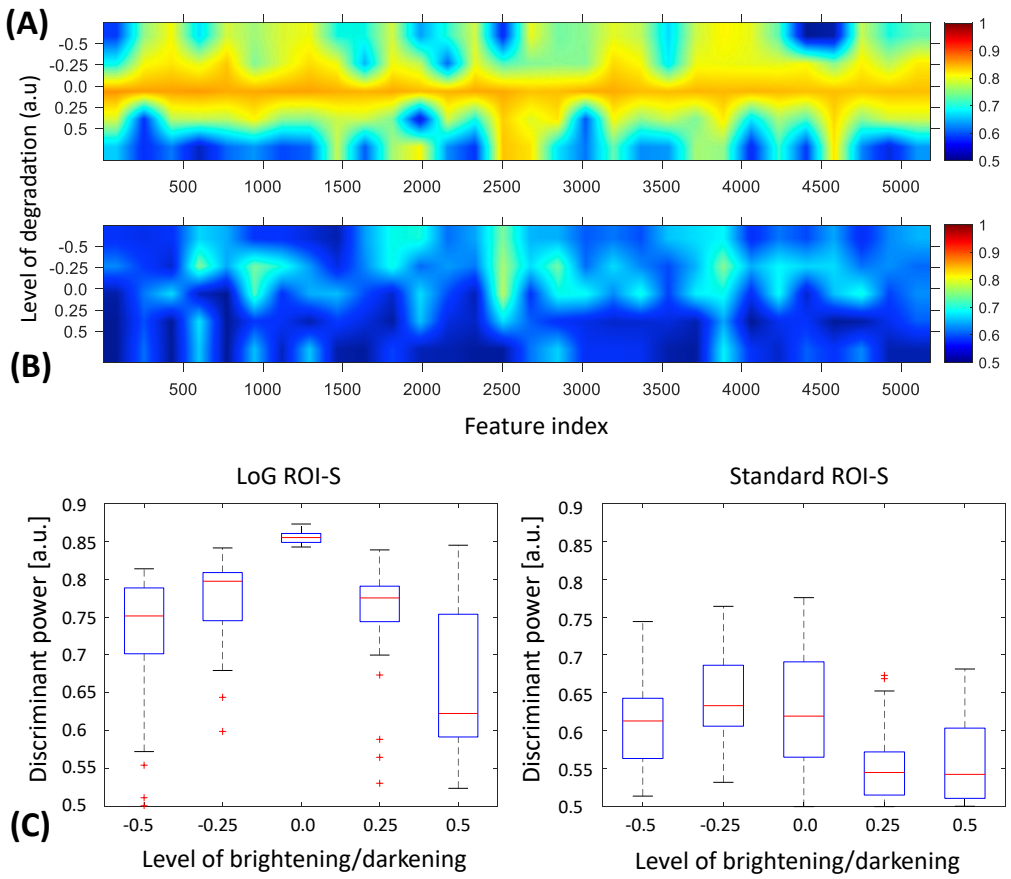


*Fig 5. Discriminant Power (DP) maps of the 30 highest performing AlexNet features computed for (A) LoG ROI-S sequences and (B) standard ROI-S, by varying (y-axis) the level of degradation for brightening/darkening in the range [-0.5,0.5]. (C) Boxplot of the DPs obtained over the 30 features for the different levels of degradation using (left) the LoG ROI-S approach and (right) the standard mode.*

*Figure 6 :*

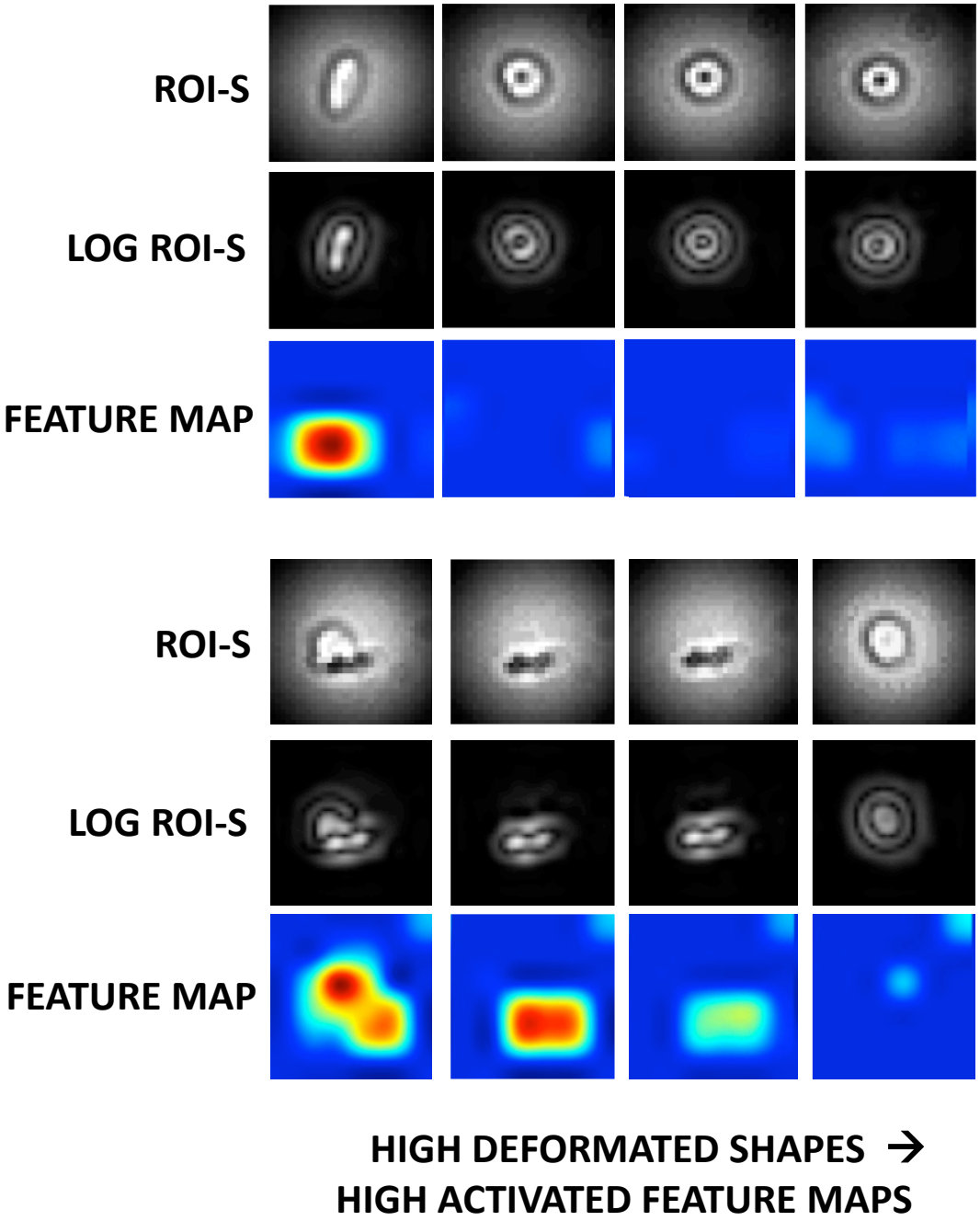


*Fig 6. Two visual examples of ROI-S for two distinct cells and related feature maps from 'pool5' of AlexNet CNN. It can be noted that the selected maps mostly activate when the cell changes shape, demonstrated to be sensitive to cell deformation. False colours are used for the sake of better visualization.*

***Figure 7:***

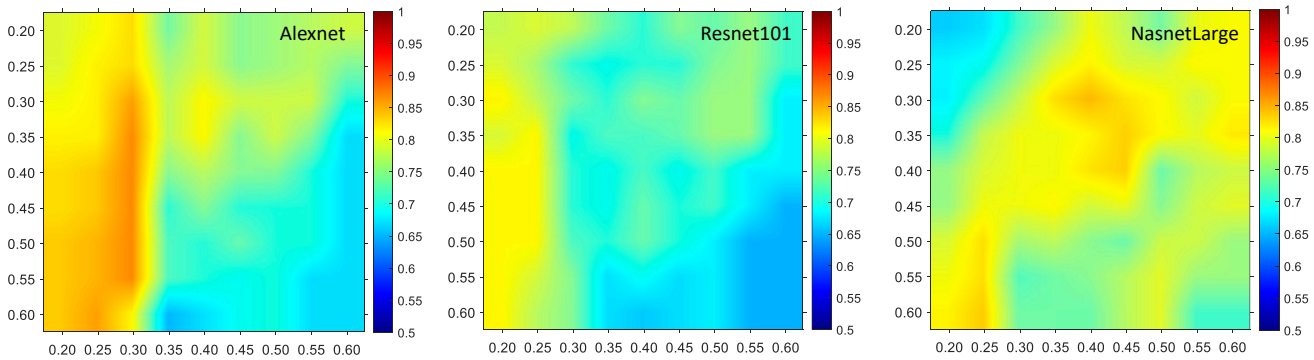


*Fig. 7 Maps of accuracy values for AlexNet, ResNet101, and NasNetLarge, for combinations of the two thresholds in the range [0.2 – 0.6]. Colors indicate the ACC values.*

***Tables:***

*Table I. Deep learning neural networks selected for the transfer learning step: size of the input frames, and layers used for the image encoding and related number of features are also indicated*

| *Deep Learning Network Name* | *Size of input frame* | *Layer used for transfer learning* | *N. of features transferred* |
|---|---|---|---|
| *AlexNet* | *227 x 227* | *'pool5'* | *9216* |
| *ResNet-101* | *224 x 224* | *'pool5'* | *2048* |
| *NasNetLarge* | *331 x 331* | *'avg_pool5* | *4032* |

*Table II. Best performance accuracy values for single-frame classification, single-threshold at frame level over the video, and two-thresholds strategy.*

| ACC | Single-frame | Single-threshold | Two-threshold |
|---|---|---|---|
| AlexNet | 81% | 85% | 88% |
| ResNet101 | 81% | 80% | 82% |
| NasNetLarge | 79% | 84% | 85% |